DOI: 10.17344/acsi.2022.7775 *Acta Chim. Slov.* **2022,** *69,* 756–771

Feature article

Adaptation of the Crystal Structure to the Confined Size of Mixed-oxide Nanoparticles

Darko Makovec

Department for Materials Synthesis, Jožef Stefan Institute, Jamova ulica 39, SI-1000 Ljubljana, Slovenia.

** Corresponding author: E-mail: darko.makovec@ijs.si*

Received: 08-29-2022

Abstract

Chemical composition and crystal structure are central to defining the functional properties of materials. But when a material is prepared in the form of nanoparticles, the structure and, as a consequence, the composition will also frequently change. Understanding these changes in the crystal structure at the nanoscale is therefore essential not only for expanding fundamental knowledge, but also for designing novel nanostructures for diverse technological and medical applications. The changes can originate from two thermodynamically driven phenomena: (i) a crystal structure will adapt to the restricted size of the nanoparticles, and (ii) metastable structural polymorphs that form during the synthesis due to a lower nucleation barrier (compared to the equilibrium phase) can be stabilized at the nanoscale. The changes to the crystal structure at the nanoscale are especially pronounced for inorganic materials with a complex structure and composition, such as mixed oxides with a structure built from alternating layers of several structural blocks. In this article the complex structure of nanoparticles will be presented based on two examples of well-known and technologically important materials with layered structures: magnetic hexaferrites ($BaFe_{12}O_{19}$ and $SrFe_{12}O_{19}$) and ferroelectric Aurivillius layered-perovskite bismuth titanate ($Bi_4Ti_3O_{12}$).

Keywords: Nanoparticles; crystal structure; hexaferrites; Aurivillius structure; layered perovskites; polymorphs

1. Introduction

The functional properties of materials change significantly when they are prepared in the form of nanoparticles. In the scientific literature these changes are usually associated with one of two fundamental reasons. The size effect can simply originate from the large surface-to-volume ratio of nanoparticles. The properties, which are defined by processes occurring on the surfaces (e.g., adsorption capacity, catalytic activity, the rate of solid-state chemical reactions, etc.) will generally improve as the particle size becomes smaller. With the explosion in research devoted to nanoscience at the beginning of this millennium, an especially large amount of attention was given to the direct effects of the confined size on some functional properties. Well-known examples are the quantum-confinement effect observed in semiconducting nanoparticles (i.e., quantum dots) and the superparamagnetism of magnetic nanoparticles. Much less attention has been given to the changes in properties that are an indirect consequence of the changes in crystal structure that are due to the restricted size of nanomaterials. This is because when the size is restricted to such an extent, the crystal structure of nanoparticles can also change significantly.

The influence of the confined size on the structure of nanoparticles can range from minor changes in atomic positions to the stabilization of diverse structural variations and metastable structural polymorphs. At the very large surface-to-volume ratios of nanoparticles, the structural changes can simply be related to the relaxation and reorganization of the atoms at the surfaces. However, the adaptation of the structure to the small size frequently cannot be explained merely by the increased surface area as it clearly affects the whole particle, including its interior.

The adaptation of the crystal structure generally involves systematic displacements of the atoms from their ordered positions and deviations in the occupation of different lattice sites. The extent of the changes in the crystalline structure that can be accommodated with the small size depends on the complexity of the composition and the crystal structure. In simple oxides the changes in the occupation of different lattice sites can be restricted to an increased content of vacancies. Classical thermodynamic calculations indicate that the size-dependent vacancy-formation energy and entropy result in an increase in the vacancy concentration at a reduced crystallite size.[1] In mixed oxides comprising different cationic lattice sites (e.g., in

cubic ferrites with a spinel structure) an additional adaptation mechanism is possible based on the changes in the distribution of constituting cations over different lattice sites.[2–6] Finally, in mixed oxides with a complex structure built from alternating layers of several structural blocks, e.g., a structure of hexagonal ferrites (hexaferrites) and the Aurivillius structures of layered perovskites, the adaptation of the crystal structure to the constricted size of the nanoparticles is dominated by the termination of the particle at its surfaces with a specific, low-energy atomic layer.[7] That can enable the synthesis of nanoparticles with a specific structure, which can be referred to as a specific structural variation of the bulk structure, stabilized at the nanoscale.[8] In addition, the changes in the crystal structure due to the confined size of the nanoparticles can lead to a deviation from the bulk composition,[5,7] or at least to an increased flexibility of the composition, i.e., the composition of the nanoparticles can change to a much larger extent without any precipitation of secondary phases when compared to the corresponding bulk.[5] Also, the solid solubility of the foreign atoms in the host crystal usually increases with a decreasing size of the nanoparticles.[1]

In addition to the above-mentioned changes in the crystal structure due to the restricted size of the nanoparticles, various metastable structural polymorphs can be stabilized at the nanoscale. Polymorphs are defined as substances that are chemically identical but exist in more than one crystal form. For example, iron(III) oxide appears in five different polymorphs: α (hematite), β, γ (maghemite), ε, and ξ.[9] The metastable polymorphs are formed during the initial stages of crystallization, because they have a lower nucleation barrier than the stable phase.[10,11] With the particle growth, a metastable polymorph usually transforms in an energetically cascading series of polymorphic stages to the equilibrium polymorph. This phenomenon is known as the Ostwald step rule.[11] However, if the metastable polymorph has a lower surface energy than the equilibrium polymorph it can remain stable while in the form of small particles with a large surface area.[10] For example, with the confined growth of iron(III) oxide nanoparticles dispersed in a silica matrix, the γ, ε, and sometimes β polymorphs appear in sequence before the transformation to the thermodynamically stable α polymorph in the larger particles resembling the bulk.[12,13] Even though the polymorphs stabilized on the nanoscale are usually referred to as "metastable", their stability can be thermodynamically explained by taking into consideration their large surface area related to their small size.[12,13] Strictly speaking, the metastable polymorphs are not a consequence of the adaptation of the crystal structure to the restricted size; however, as they only appear at the nanoscale they can be considered in the context of the size effect.

Metastable polymorphs stabilized at the nanoscale are abundant among simple oxides. Well-known examples of polymorphs for which the stability changes with the nanoparticle size include titania (anatase→brookite→rutile), zirconia (monoclinic→tetragonal), alumina (γ→α), silica (tridymite→cristobalite→quartz), and many others. The polymorphism is technologically very important, as different polymorphs of the same stoichiometry can have vastly different functional properties, and many metastable polymorphs represent very important functional nanomaterials. Iron(III) oxide can be used as a good illustration of the diversity of magnetic properties for different polymorphs.[9] The thermodynamically stable phase hematite (α-Fe_2O_3) is only weakly magnetic. The metastable maghemite (γ-Fe_2O_3) is soft magnetic with a relatively high saturation magnetization, and maghemite nanoparticles are actually the most frequently used magnetic nanoparticles, especially in medicine.[14] In contrast, ε-Fe_2O_3 is hard magnetic as it exhibits the largest coercive field among all the oxides. The β-Fe_2O_3 and ξ-Fe_2O_3 phases are antiferromagnetic.[9]

Even though the Ostwald step rule should not be restricted to simple oxides, reports of polymorphs stabilized at the nanoscale are very scarce for inorganic materials with a complex composition and crystal structure, such as mixed oxides with several constituting ions distributed over many non-equivalent lattice sites within a large unit cell. Such complex materials include mixed oxides with a layered structure, which are the topic of this article.

Finally, in contrast to the thermodynamically driven adaptations of the structure to the small size mentioned so far, nanomaterials can exhibit a specific crystal structure because of the reaction kinetics during their synthesis. Usually, mild synthesis conditions, e.g., a low temperature, are used during the synthesis of the nanoparticles to limit the particle growth. Such specific, non-equilibrium synthesis conditions can also contribute to deviations from the regular, bulk structure when the material is synthesized in the form of nanoparticles.

In this feature, article the thermodynamically driven adaptations of the crystal structure to the small size of the nanoparticles will be presented using two examples of mixed-oxide nanoparticles with a structure built from alternating layers of two structural blocks: a hexaferrite ($BaFe_{12}O_{19}$ and $SrFe_{12}O_{19}$) and an Aurivillius layered-perovskite bismuth titanate ($Bi_4Ti_3O_{12}$). The mixed oxides with a layered structure represent technologically important materials. The hexaferrites exhibit extraordinary magnetic properties dominated by a very large magnetocrystalline anisotropy constant. As ceramics they represent the most abundant materials (by volume) used today for permanent magnets and are also used in microwave devices and absorbers.[15] In the form of nanoparticles, hexaferrites enabled the development of some entirely new types of materials, including the first ferromagnetic fluids (i.e., liquid magnets),[16,17] and novel magneto-responsive suspensions[18,19] and polymer composites.[20] Hexaferrite nanoparticles were also tested in novel applications, e.g., in novel spin-memory devices[21,22] and in medical applications.[23,24] Layered-perovskite phases of the Aurivillius family ($(Bi_2O_2)(A_{n-1}B_nO_{3n+1})$), where A is a large

12-coordinated cation, and B is a small 6-coordinated cation), the Ruddlesden-Popper family ($A'_{n-1}A''_2B_nO_{3n+1}$, where A' and A'' are alkali, alkaline earth or rare-earth ions) and the Dion-Jacobson family ($A''(A'_{n-1}B_nO_{3n+1})$) possess interesting properties such as ferroelectricity, colossal magnetoresistance, catalytic activity and superconductivity. The Aurivillius $Bi_4Ti_3O_{12}$ ceramics are promising materials for ferroelectric random-access-memory devices and lead-free, high-temperature piezoelectric and pyroelectric devices.[25] $Bi_4Ti_3O_{12}$ nanoparticles were tested for biomechanical energy harvesting,[26] sensing,[27,28] visible-light photocatalysis,[29,30] electrocatalysis,[28] and piezocatalysis.[31,32] Technologically important families of layered mixed oxides further include high-temperature superconducting cuprates,[33] and lithium and sodium transition-metal layered oxides ($LiMO_2$ and Na_xMO_2, M = transition metal), which are used as the cathode materials in batteries.[34,35] In all these materials we can expect that similar mechanisms will govern the adaptation of the crystal structure to the nanoscale.

Attempts to study the adaptation of such complex crystal structures to the restricted sizes of nanoparticles have seldom been reported in the scientific literature. To the best of our knowledge also, the metastable polymorphs of layered mixed oxides stabilized at the nanoscale were not reported prior to our work. The reason is primarily related to the difficult synthesis of such complex materials in the form of small nanoparticles, which usually involves high temperatures that lead to the rapid growth of particles and favour thermodynamically stable phases. The hydrothermal method is one of the few methods enabling the direct synthesis (without a calcination stage) of layered mixed oxides, such as hexaferrites and bismuth titanate. The method involves the precipitation of the constituting cations from the aqueous solutions with a strong hydroxide, usually NaOH, followed by a hydrothermal treatment, i.e., the alkaline aqueous suspension of the precipitated hydroxides is heated in a closed autoclave at an elevated temperature (typically around 200 °C) and an equilibrium water pressure.[36]

On the other hand, the characterization of small nanoparticles with a complex structure is very challenging. Conventional methods based on x-ray diffraction (XRD) are not efficient for the characterization of small nanoparticles. In our research we combined direct atomic-resolution high-angle annular dark-field (HAADF) imaging with a probe spherical-aberration corrected scanning-transmission electron microscope (STEM) with other microscopy techniques (energy-dispersive X-ray spectroscopy (EDXS), electron-energy-loss spectroscopy (EELS)) and XRD to examine the nanoparticle structures. HAADF imaging enables "Z-contrast", as the intensity of the spots representing individual atomic columns in the atomic resolution images of the crystal depends on the column's average atomic number Z (~Z^{α} with α slightly lower than 2).[37] Thus, the columns occupied by the heavy cations (Ba^{2+}, Sr^{2+}, Bi^{3+}) can be clearly resolved from the columns of the lighter cations (Fe^{3+}, Ti^{4+}) (the O^{2-} columns are too light to be visible in HAADF images).

2. Structure of Barium and Strontium Hexaferrite Nanoplatelets

2. 1. Magnetoplumbite Structure

Barium hexaferrite ($BaFe_{12}O_{19}$, or BHF) and strontium hexaferrite ($SrFe_{12}O_{19}$, or SHF) are the simplest members of a large family of hexagonal ferrites (i.e., hexaferrites) that can be formed by repeatedly stacking layers of three structural building blocks: the "S" block ($MeFe_4O_8$, where Me denotes either a divalent (e.g., Zn^{2+}, Co^{2+}) or trivalent (Fe^{3+}) ion), the "R" block (AFe_6O_{11}, where A denotes a large divalent ion Ba^{2+}, Sr^{2+}, or Pb^{2+}), and the "T" block ($A_2Fe_8O_{14}$), along the *c*-axis of the hexagonal structure. The BHF and SHF are also known as M-type hexaferrites. They represent the simplest members of the hexaferrite family with a magnetoplumbite structure composed of only Ba^{2+}/Sr^{2+} ions and Fe^{3+} ions arranged in the hexagonal "R" block ($(BaFe_6O_{11})^{2-}$) and the cubic "S" block ($(Fe_6O_8)^{2+}$) (Note that the magnetoplumbite structure is frequently simply referred to as the "hexaferrite" structure). The unit cell (S.G.: *P*63/*mmc*, a = 5.88 Å, c = 23.18 Å) can be illustrated by the RSR^*S^* stacking sequence, where the asterisk denotes the rotation of the block by 180° around the hexagonal *c*-axis. Within the structure, the Fe^{3+} ions occupy five different lattice sites, i.e., one tetrahedral ($4f_1$), three octahedral (12k, 2a, $4f_2$), and one trigonal (2b) (see Figure 2(a)).[15] Due to the anisotropic, layered structure, the growth of the hexaferrite crystals is limited in the *c*-direction, resulting in nanoparticles growing in the form of thin hexagonal platelets., i.e., nanoplatelets (NPL).[16]

2. 2. Hydrothermal Synthesis of Hexaferrite Nanoplatelets

Hexaferrite nanoplatelets can be efficiently synthesized using a simple and scalable hydrothermal method.[7,18,39–45] This method is based on the hydrothermal treatment of an aqueous suspension of the corresponding hydroxides in the presence of a high concentration of hydroxyl ions. An excess of Ba^{2+}/Sr^{2+} ions is used to avoid the parallel formation of hematite. After the hydrothermal treatment the product is washed with a dilute acid to dissolve any Ba/Sr-rich compounds that formed due to the excess Ba/Sr. Ba- and Sr-rich compounds (e.g., $BaCO_3$(s), $SrCO_3$(s)) are all very soluble, whereas the hexaferrite is completely insoluble.[7,39–42,45]

The evolution of the morphology of the formed NPLs during hydrothermal synthesis is very similar for the two hexaferrites: BHF and SHF. The primary, ultraf-

ine discoid NPLs, around 10 nm wide and less than 3 nm thick, already form at temperatures below 100 °C (given a sufficient time for the hydrothermal treatment) (Figure 1). The ultrafine NPLs exhibit weak magnetic properties. With an increased temperature of the hydrothermal treatment, the size of the NPLs remains almost constant up to approximately 150 °C, when individual NPLs start to grow with the mechanism of Ostwald ripening (Figure 1). With Ostwald ripening the NPLs obtain their characteristic shape of hexagonal platelets, which reflects their hexagonal structure. And only after the Ostwald ripening do the NPLs obtain their hard-magnetic properties with a sizable saturation magnetization, characteristic for hexaferrites. The Ostwald ripening (sometimes also referred to as a secondary recrystallization) is a special mechanism, where individual particles grow very rapidly at the expense of other particles, which dissolve. Because of this very rapid growth, the phenomenon is also referred to as anomalous or exaggerated growth. The size of particles that grow exaggeratedly is very difficult to control. Hexaferrite NPLs with a size below 100 nm can only be obtained if the hydrothermal treatment is stopped immediately after the start of the exaggerated growth. If the exaggerated growth is allowed to proceed, the widths of the platelets rapidly exceed 1 μm, while their thickness increases much more gradually (Figure 1).[7,39] The exaggerated growth can be regulated to some extent with chemical substitutions. For example, if the Fe^{3+} in the composition of the BHF is partially substituted with Sc^{3+}, the exaggerated growth is suppressed to some extent, enabling the controlled synthesis of NPLs with a relatively narrow distribution of widths centred around 50 nm.[42,44] Alternatively, the growth of NPLs can be mediated with appropriate surfactants, such as oleic acid.[39]

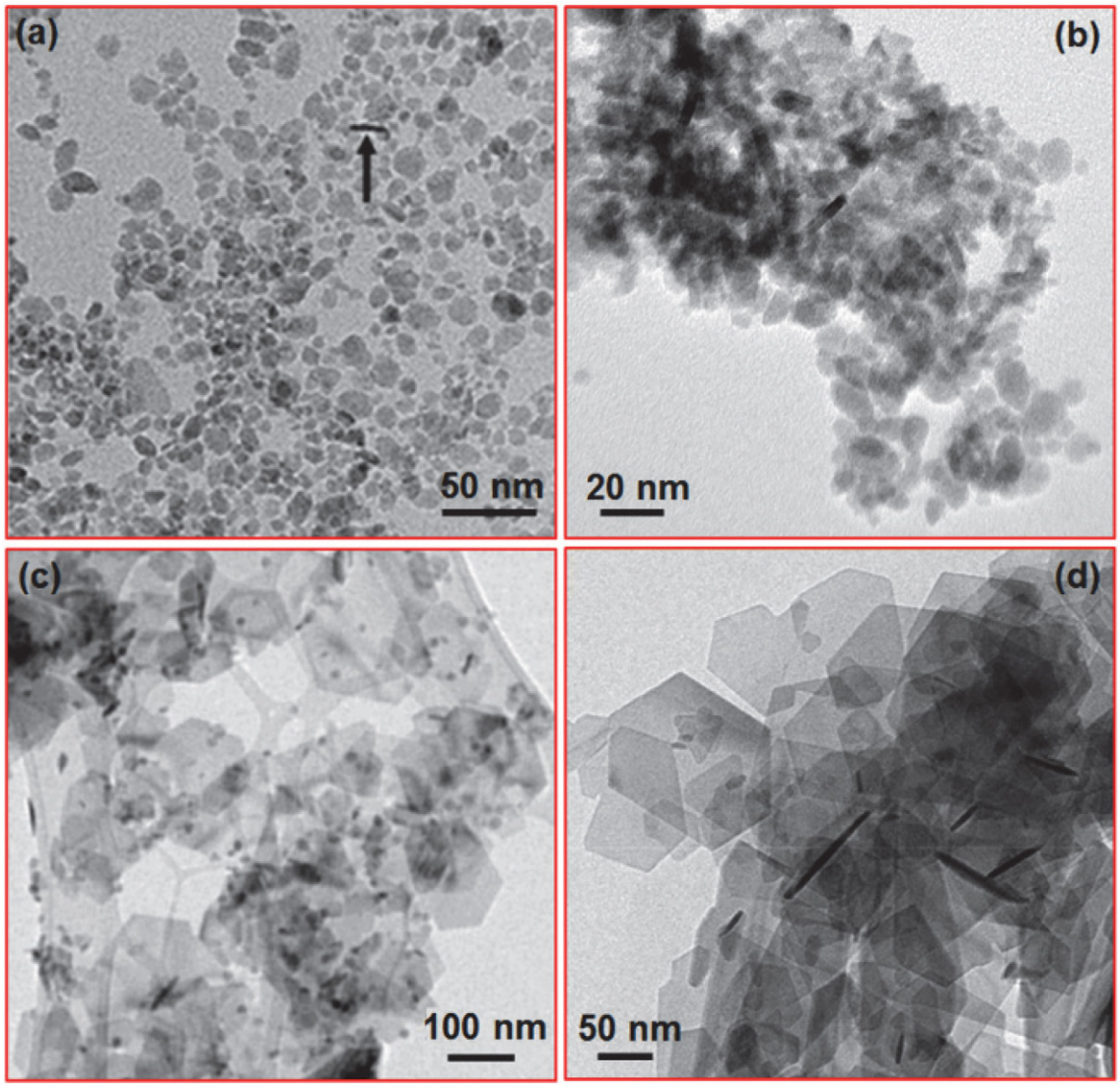

Figure 1. TEM micrographs of the BHF NPLs hydrothermally synthesized for 24 hours at 80 °C (a), and by heating the autoclave to 150 °C (b), 160 °C (c), and 200 °C (d).

2. 3. Structure of Hexaferrite Nanoparticles Obtained by Exaggerated Growth

For the hydrothermal synthesis of hexaferrite NPLs with applicable magnetic properties the exaggerated growth is necessary; however, it must be stopped before the NPLs grow too large. Usually, the NPLs with widths below 100 nm are required for various applications.[42,44] For widths around 100 nm, the hexaferrite NPLs remain very thin, i.e., their thickness remains less than two unit-cell parameters of their hexagonal structure in the corresponding *c*-direction (c = 23.18 Å). Already after analyses of the first successfully synthesized NPLs with a high-resolution transmission electron microscope (HRTEM) they appear to exhibit a specific structure. For the small thickness it seemed logical that their layered structure will be terminated at the basal surfaces always at the same, low-energy crystal plane. In the layered structure, such a specific structure should also result in a deviation from the bulk composition. For example, if the hexaferrite NPLs were to terminate at the basal surfaces with the Ba-containing planes, their composition would be Ba-rich, and vice versa. However, our analyses of the BHF NPLs' structure with a combination of XRD, X-ray absorption fine structure (XAFS), Mössbauer spectroscopy, HRTEM, and EDXS could not unambiguously confirm this hypothesis.[46] The structure of the BHF NPLs was revealed later, when we applied HAADF imaging with a STEM.[8]

Figure 2 (b) shows a HAADF STEM image of an exaggeratedly grown BHF NPL oriented edge-on, i.e., with the basal surfaces parallel to the electron beam. The Ba-containing columns can be clearly resolved from the lighter Fe columns. The positions of the cations in the projected magnetoplumbite structural model are superimposed over the experimental image of Figure 2 (b) to reveal the NPL structure. The NPL in Figure 2 (b) contains only two Ba-containing R structural blocks and its cationic sublattice terminates at the basal surfaces with a layer of Fe ions at the octahedral Fe(12k) sites, i.e., with the complete S structural block. It should be noted that the oxygen columns are not visible on the HAADF images. However, it is expected that the NPLs' structure is terminated with an oxygen-terminating layer in the air.

An analysis of a large number of NPLs showed that the NPLs with widths below 100 nm usually contained only two R blocks. Only seldom did the BHF nanoplatelets contained three or four R blocks. However, the cationic sublattice of the NPLs' structure always terminated at the basal surfaces with the same, Fe(12k) lattice plane. The content of the R blocks and the specific termination of the NPLs' structure determine their thickness: the NPL containing two R blocks is ~3.1 nm thick. Moreover, all the NPLs of equal thickness have basically the same structure across the NPL. The structure of a NPL containing two R structural blocks can be represented by the SRS*R*S stacking sequence across the NPL. With growth, the thickness of the NPLs cannot increase continuously, but in a discrete, stepwise manner, by gradually adding the SR segments.[7,8] The structure of exaggeratedly grown SHF NPLs was similar to that of the BHF NPLs.[45]

Due to the specific structure the hexaferrite NPLs display a different composition than the $BaFe_{12}O_{19}$ bulk. The composition of a NPL containing the two R blocks (SRS*R*S stacking) corresponds to the theoretical composition $BaFe_{15}O_{23}$. This theoretical composition was confirmed by a quantitative EDXS analysis. With increasing thickness, the nanoplatelet composition gradually approaches that of the bulk.[7,8,45] Note that although the the-

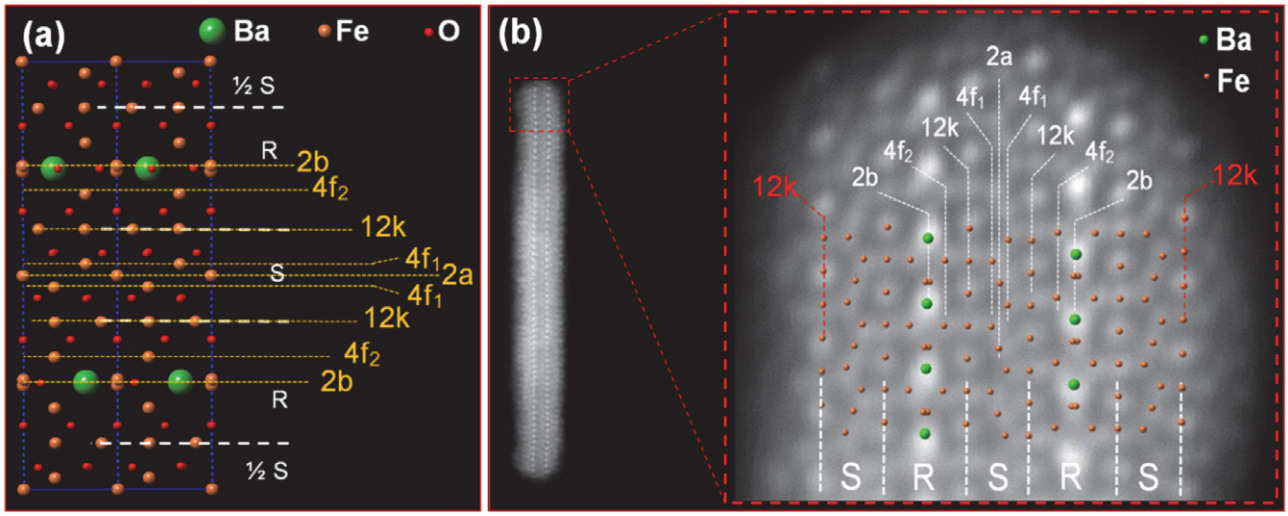

Figure 2. A schematic representation of the magnetoplumbite structure (a) and HAADF STEM image of a hexaferrite nanoplatelet oriented along the <10$\bar{1}$0> direction of its magnetoplumbite structure (b). In image (b) the projected magnetoplumbite structure is superimposed to illustrate the positions of the Ba^{2+} and Fe^{3+} columns. Different Fe lattice sites (trigonal 2b, tetrahedral $4f_1$, octahedral 12k, 2a, and $4f_2$) are marked. (*Reproduced from the publication[44] by D. Makovec, M. Komelj, G. Dražić, B. Belec, T. Goršak, S. Gyergyek, D. Lisjak, Acta Mater.* ***2019****, 172, 84–91 under the terms of CC BY 4.0 license*).

oretical composition of the nanoplatelets containing two R blocks is equal to the composition of the Fe^{2+}-containing X-type hexaferrite $Ba_2Fe^{2+}{}_2Fe^{3+}{}_{28}O_{46}$, the stacking of the structural blocks in the X-type hexaferrite is different ($RSRSSR^*S^*R^*S^*S^*$) and its unit cell is much larger (c = 84.1 Å) than the thickness of the nanoplatelet.[47] Moreover, the specific composition of the thin NPLs is not related to the change in the oxidation state of Fe ions. The experimental determination of Fe valence state of the NPLs using an analysis of the EELS spectra showed the Fe valence to be close to 3+.[7]

The termination of the NPLs' structure at the basal surfaces was found to depend on the conditions applied during their preparation. The S-block-terminated structure was actually only found in the NPLs washed with diluted acid after the hydrothermal synthesis (Figure 3 (b)).[7,8] If the nanoplatelets were extracted from the reaction mixture before the washing step, they were terminated at the basal surfaces with the Ba/O/Fe(2b) mixed planes (Figures 3 (a) and (c)). Interestingly, during the washing not only was the top Ba-containing plane dissolved, but also the first Fe plane beneath (Fe($4f_2$)) was dissolved from the surface to reveal the S-terminated structure (Figure 3 (a)).[7]

Experimental observations of the NPLs' structure termination were supported with *ab initio* calculations of the relative stability of different terminations of the BHF performed using the density functional theory (DFT). The first calculations of a periodic structure resembling the bulk were performed by Matej Komelj from the Jožef Stefan Institute, Ljubljana, Slovenia. These calculations suggested that in energy terms the most stable surface lay-

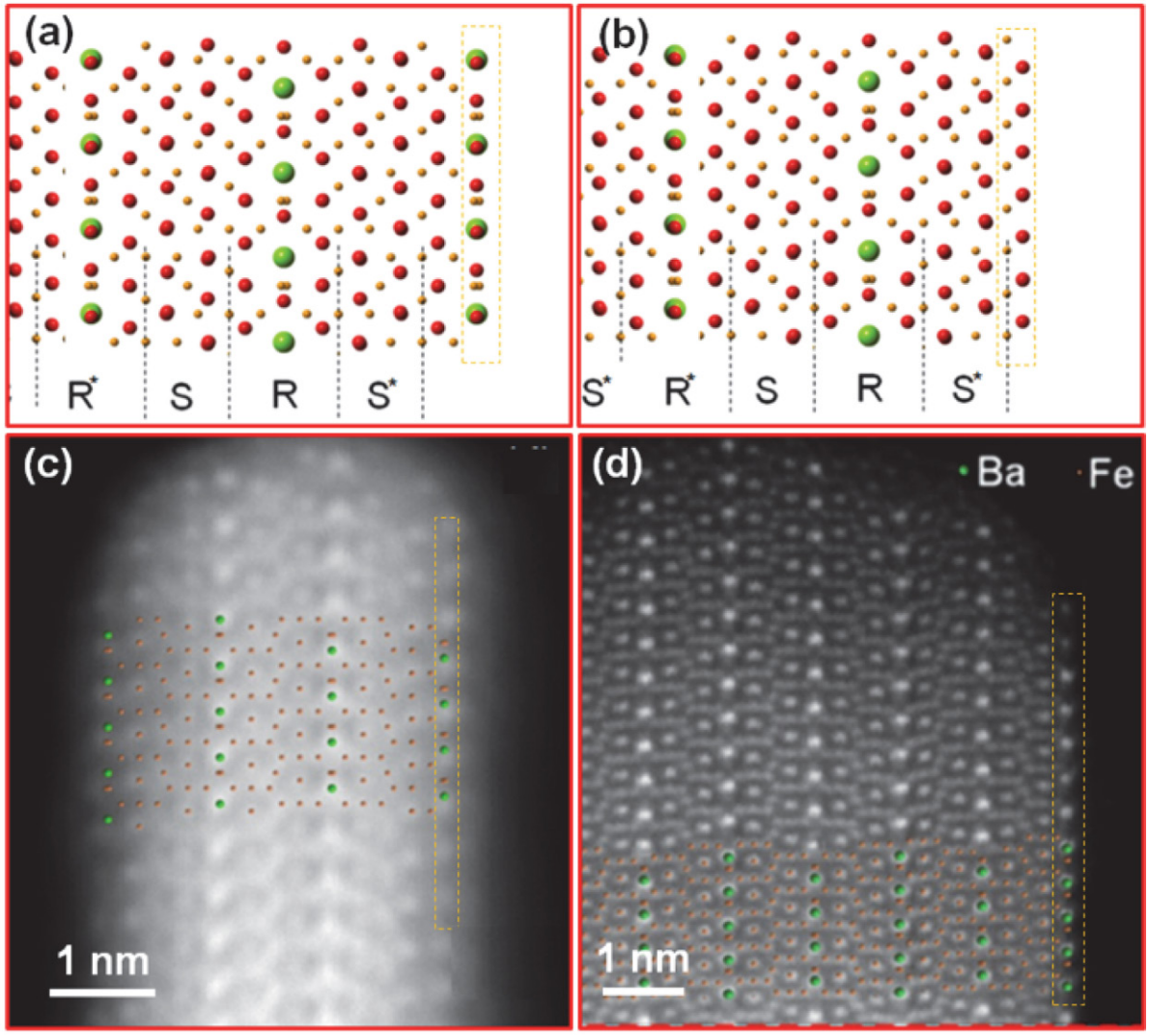

Figure 3. Two structural models schematically representing the structure across the hexaferrite NPL before (a) and after (b) washing with dilute nitric acid. Figures (c) and (d) show HAADF STEM images of BHF NPLs after washing with diluted acid (c) and after annealing for 2 hours at 700 °C. The projected magnetoplumbite structure is superimposed over the images (c) and (d) to illustrate the positions of the Ba^{2+} and Fe^{3+} columns. The termination layer at the basal surfaces of the NPLs is marked with a yellow rectangle. (*Adapted from the publication by D. Makovec, B. Belec T. Goršak, D. Lisjak, M. Komelj, G. Dražić, S. Gyergyek, Nanoscale 2018, 10, 14480–14491 with permission from The Royal Society of Chemistry.*[7])

er is obtained with a termination of mixed Ba/O/Fe(2b) planes.[8] Such a structure was observed experimentally when the NPLs were annealed at high temperatures. Figure 3(d) shows an atomic-resolution HAADF STEM image of the platelet crystal obtained by annealing the BHF NPLs at 700 °C. At that high temperature the NPLs grew to larger, plate-like crystals resembling the bulk. At their flat, basal surfaces they were clearly terminated with the Ba-containing planes.[7] The difference in the termination of the structure between the NPLs and the larger crystals after annealing highlights the crucial role of the chemical environment, which was not taken into the consideration during the calculations. We must bear in mind that the NPLs after the hydrothermal synthesis are suspended in an aqueous solution containing high concentrations of different ions, mainly originating from an excess amount of Ba^{2+} ions and a high concentration of NaOH, hydrating the surfaces.

Later, the *ab initio* calculations were extended to thin structures, which resembled the structure of the primary nanoplatelets.[7] The calculations of the relative stability of thin structures symmetrically terminating at both basal surfaces at different lattice planes showed the highest stability for a structure terminated with the O layers above the Fe($4f_1$) of the S block; however, its stability was just slightly higher than the termination at the O-only layers above the Fe(12k) layers, experimentally determined as the termination layers for the washed BHF nanoplatelets.

Recently, detailed DFT calculations were performed by the group from Scuola Internazionale Superiore di Studi Avanzati (SISSA), Trieste, Italy, led by Layla Martin-Samos. Their calculations clearly demonstrated the influence of the chemical environment on the equilibrium structure of BHF NPLs. In the absence of water (and other species), the calculations showed that the structure terminating with the mixed Ba/O/Fe(2b) planes is the most stable. The same surface is also the most stable in oxygen/iron-poor (Ba-rich) conditions, whereas the fully hydroxylated 12k-O surface is the most stable in oxygen/iron-rich conditions, in line with the experimental observations.[48]

In conclusion, the BHF and SHF NPLs synthesized via exaggerated growth (i.e., Ostwald ripening) during the hydrothermal treatment show specific structures and compositions, defined by the termination of the particle at its surfaces with a specific, low-energy atomic layer. The termination layer depends on the chemical environment. As the structure and composition of hexaferrite NPLs are significantly different from the bulk, they can be considered as a novel structural variation of the hexaferrites stabilized on the nanoscale. An equivalent adaptation mechanism can also be expected for other mixed oxides with a layered structure when they are synthesized in the form of thin NPLs.

2. 4. Structure of Primary Hexaferrite Nanoplatelets

The NPLs that grow exaggeratedly during the hydrothermal synthesis exhibit the same crystal structure for both the hexaferrite analogues: BHF and SHF. In contrast, the primary NPLs, i.e., the nanoparticles that appeared as the first product in the initial stage of the hydrothermal synthesis, exhibit a completely different structure for the two hexaferrite analogues, even though they had a similar discoid morphology. Atomic-resolution HAADF STEM imaging showed that the washed primary BHF NPLs exhibit a specific variation of the magnetoplumbite structure – the smallest possible structural segment still maintaining the hexaferrite motif. Figure 4 shows a HAADF STEM im-

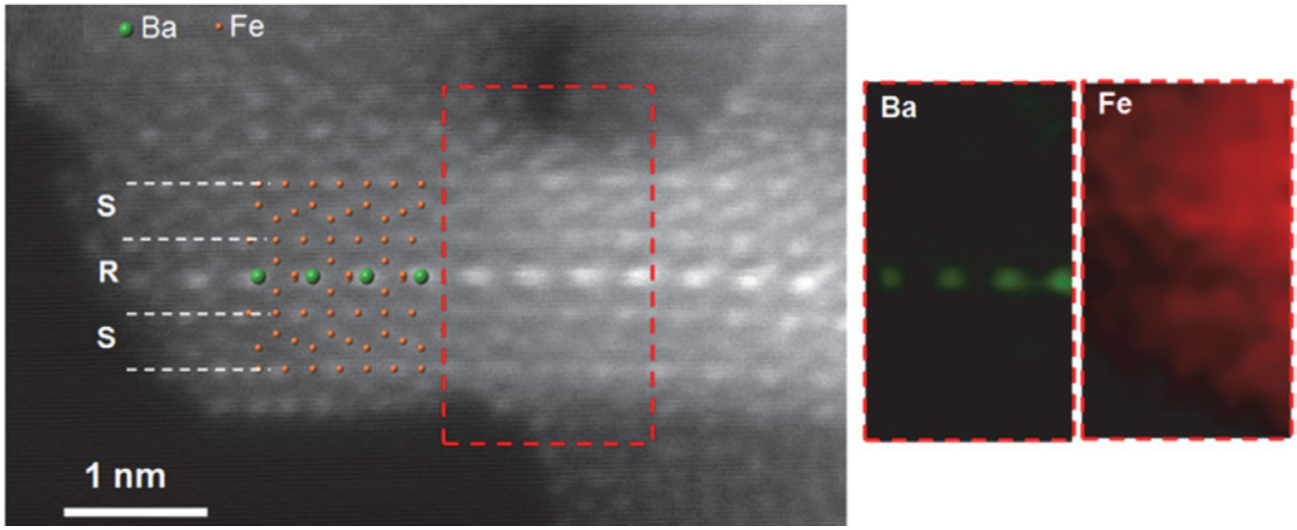

Figure 4. HAADF STEM images of a primary BHF NPL with corresponding EELS elemental maps for Ba and Fe (the area of the analysis is marked on the image with a red rectangle). An SRS* segment of the hexaferrite structure projected along the <10$\bar{1}$0> direction is superimposed over the image to illustrate the positions of the Ba^{2+} and Fe^{3+} ions. (*Adapted from the publication by D. Makovec, B. Belec T. Goršak, D. Lisjak, M. Komelj, G. Dražić, S. Gyergyek, Nanoscale 2018, 10, 14480–14491 with permission from The Royal Society of Chemistry.*[7])

age of a primary BHF NPL oriented edge-on. Even though the NPL is not perfectly oriented along the zone axis and an additional layer of adsorbed atoms is visible on its surfaces, its structure is composed of only one Ba-containing R structural block sandwiched between the two S blocks. The thickness of the SRS*-structured NPLs is therefore less than the dimension of one magnetoplumbite SRS*R* unit cell. Their composition is significantly enriched in Fe compared with the theoretical composition corresponding to the chemical formula $BaFe_{18}O_{28}$.[7] Note, that the theoretical composition of the SRS*-structured primary BHF nanoplatelets is equal to the composition of the Fe^{2+}-containing W-type hexaferrite ($BaFe^{2+}{}_2Fe^{3+}{}_{16}O_{27}$) with different stacking of the structural blocks (SSRS*S*R*).[47]

Even though the structure and composition of the primary BHF NPLs strongly deviates from the bulk, their structure remains a specific variation of the hexaferrites. Their structure can therefore be understood in the context of the adaptation of the magnetoplumbite structure to the restricted size.

In contrast to the primary BHF NPLs, the primary SHF NPLs display an entirely different structure. Already during our first study devoted to the hydrothermal synthesis of SHF NPLs we noticed that the structure of the primary SHF NPLs deviates from the magnetoplumbite structure. HRTEM images showed a dominant periodicity across the primary SHF NPLs that was considerably smaller (~ 9 Å) than that for the magnetoplumbite (11.5 Å corresponding

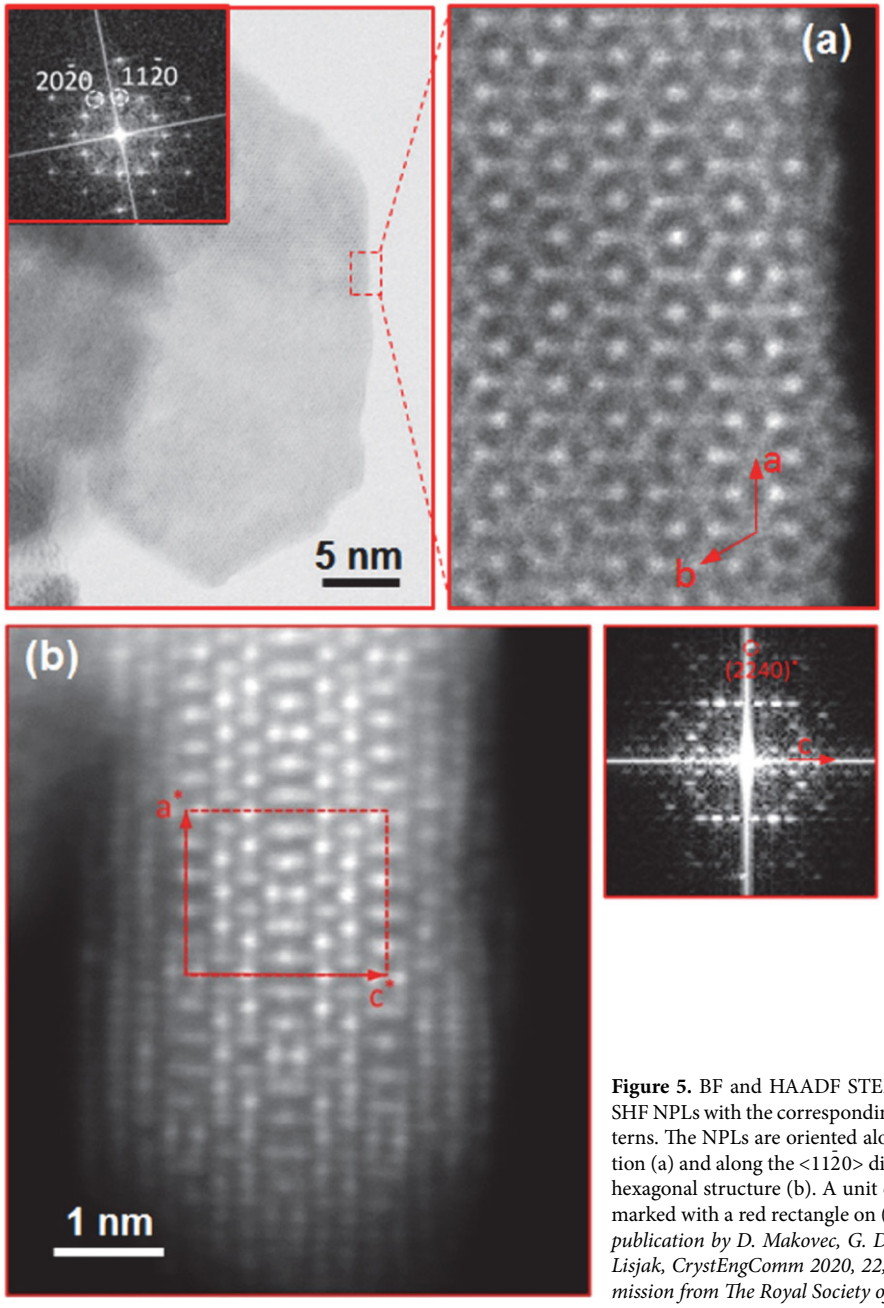

Figure 5. BF and HAADF STEM images of primary SHF NPLs with the corresponding calculated FFT patterns. The NPLs are oriented along the <0001> direction (a) and along the $<11\bar{2}0>$ direction of its complex hexagonal structure (b). A unit cell of the structure is marked with a red rectangle on (b). (*Adapted from the publication by D. Makovec, G. Dražić, S. Gyergyek, D. Lisjak, CrystEngComm 2020, 22, 7113–7122 with permission from The Royal Society of Chemistry.*[45])

to (0002)).[41] However, the NPLs were too small for any reliable structural analysis with conventional methods (e.g. XRD). Later, direct atomic-resolution HAADF STEM imaging showed that the primary SHF NPLs exhibit an exotic layered hexagonal structure, not reported before (Figure 5).[45] Due to the severe complexity of the new structure and the small thickness of the NPLs, we were not able to propose a specific structural model. However, it was evident that the new layered structure is not a variation of the hexaferrite structure. The structure was described with HAADF STEM images having an unusually large unit cell. A basic periodicity unit cell with $a^* \approx 28.3$ Å, $c^* \approx 18.0$ Å is marked on the atomic-resolution HAADF image taken along the <11$\bar{2}$0> direction (Figure 5(b)), however the atomic-resolution images along the <10$\bar{1}$0> direction suggested doubling of the unit cell in the *a*-direction.[45] Along the *c*-direction, the structure is composed of five layers of cations: three neighbouring layers containing Fe^{3+} and Sr^{2+} ions are separated by two Fe^{3+}-only layers. The structure of the discoid NPLs always terminates at the basal surfaces with an Fe^{3+}-only layer. The EDXS analysis showed an Fe-rich composition when compared to the $SrFe_{12}O_{19}$ bulk. When the primary SHF NPLs were annealed above 500 °C they grew and transformed into the magnetoplumbite structure.[45]

The complex structure of primary SHF NPLs cannot be formed because of the adaptation of the magnetoplumbite structure to the restricted size. It is clearly a metastable polymorph of the SHF stabilized at the nanoscale. It can, therefore, be explained in the context of the Ostwald step rule, where the phases with a lower thermodynamic stability form in the initial stages of the synthesis because of the lower nucleation barrier. With the growth of the nanoparticles at high temperatures the metastable polymorph transforms into the thermodynamically stable magnetoplumbite structure.

In conclusion, the primary NPLs, which appear as the first crystalline products of the hydrothermal synthesis, exhibit different structures for the two hexaferrites. The structure of the primary BHF NPLs is an SRS* variation of the SRS*R* magnetoplumbite structure, whereas the primary SHF NPLs exhibit a different, complex layered structure, which is a metastable polymorph of the SHF. The striking difference in the structure of the primary NPLs can be related to the thermodynamic stability of the two hexaferrites. The stability of the $AFe_{12}O_{19}$ hexaferrites decreases with the decreasing size of the A ion in the series: $Ba^{2+} > Sr^{2+} > Ca^{2+}$.[15]

3. Structure of Bismuth Titanate Nanoplatelets and Nanowires

3. 1. Aurivillius Structure

Bismuth titanate ($Bi_4Ti_3O_{12}$, or BIT) belongs to an Aurivillius ($(Bi_2O_2)(A_{n-1}B_nO_{3n+1})$) family of layered perovskites. Its layered structure derives from the high-temperature paraelectric phase of tetragonal *I*4/*mmm* symmetry, composed of two alternating layers: a $(Bi_2O_2)^{2+}$ layer and a perovskite $(Bi_2Ti_3O_{10})^{2-}$ layer stacked along the pseudo-tetragonal *c*-axis (see Figure 7(a)). With the onset of ferroelectricity below the Curie temperature ($T_C \sim$ 675 °C the BIT structure is slightly distorted to monoclinic symmetry *P*1*a*1 with parameters $a = 5.411$ Å, $b = 5.448$ Å, $c = 32.83$ Å.[49]

3. 2. Hydrothermal Synthesis of Bismuth-Titanate Nanoplatelets and Nanowires

BIT can be successfully synthesized with the hydrothermal treatment of an aqueous suspension of precipitated Bi^{3+} and Ti^{4+} ions in mineralizer hydroxide (NaOH or KOH) with a moderate concentration.[27,28,30–32,50–53] The synthesized BIT nanoparticles appear in a wide variety of different nano-morphologies, including 2-D platelet crystals, (i.e., rectangular nanoplatelets and nanosheets),[27,28,32,50,52,53] 1-D crystals (e.g., nanowires, nanobelts, nanobundles, nanorods),[27,28,51–53] and 3-D nanostructures assembled from 1-D or 2-D nanoparticles.[30,31,51] Our research showed that the morphologies of the product particles crucially depend on the concentration of the mineralizer hydroxide.[52] The nanowires (NWs) formed when the precipitated ions were hydrothermally treated in aqueous solutions of NaOH with lower concentrations, whereas the nanoplatelets (NPLs) were obtained at higher NaOH concentrations. For example, the hydrothermal treatment for 38 hours at 200 °C produced NWs (from 15 nm to 35 nm wide and from several hundreds of nm to several μm long) in 0.5 mol/L NaOH, whereas the rectangular NPLs (approximately 10 nm thick and from 50 nm to 200 nm wide) were synthesized in 2-mol/L NaOH (Figure 6 (a) and (b)). The NWs formed as the first crystalline BIT phase in the initial stages of the hydrothermal treatment independently of the NaOH concentration. Initially, the BIT NWs appeared together with globular aggregates of nanocrystallites with a highly defected perovskite structure. The subsequent morphology evolution depended on the concentration of the hydroxide, which influences the stability of the different phases and the kinetics of the hydrothermal reactions. At lower NaOH concentrations the NWs grew with the treatment temperature/time, while the perovskite aggregates dissolved. At the higher NaOH concentrations, the nanowires dissolved, while the NPLs grew epitaxially on the surfaces of the aggregated perovskite nanocrystallites (Figure 6 (c)).[52]

3. 3. Structure of Bismuth-Titanate Nanoplatelets

The plate-like shape of the hydrothermally synthesized BIT rectangular NPLs is consistent with their pseudo-tetragonal layered Aurivillius-type structure. Figure 7

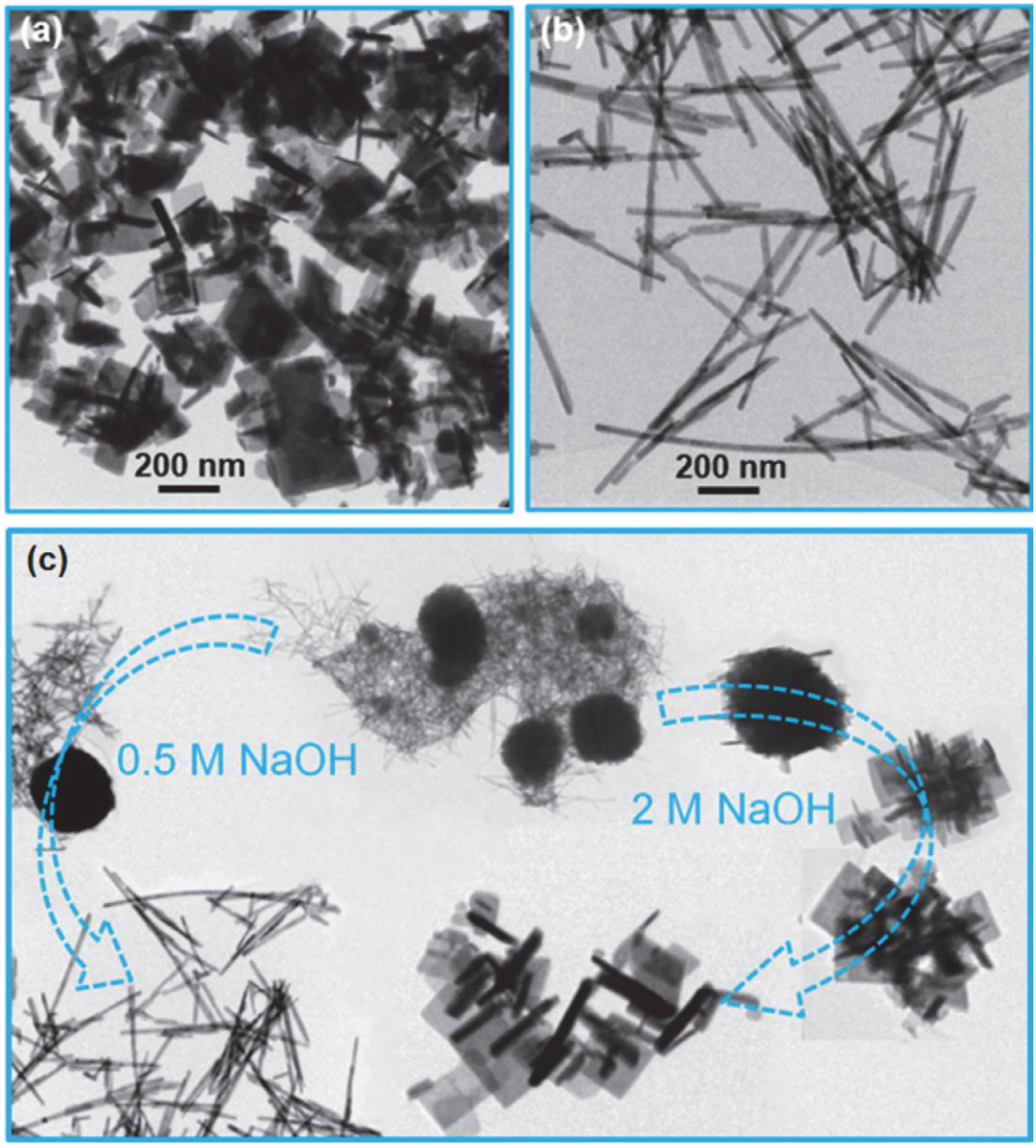

Figure 6. TEM images of bismuth-titanate NPLs (a) and NWs (b) synthesized with hydrothermal treatment of the precipitated Bi and Ti ions for 38 hours at 200 °C in the aqueous solution of NaOH with the concentration of 2 mol/L and 0.5 mol/L, respectively. (c) A schematic presentation of the morphology evolution during hydrothermal synthesis. Independently of the NaOH concentration, a mixture of NWs and globular nanocrystalline particles with a defected perovskite structure forms first. With temperature/time of the treatment in NaOH with a lower concentration, the perovskite aggregates dissolve, while the NWs grow. At a higher NaOH concentration, the NWs dissolve, while on the surfaces of the perovskite aggregates the NPLs grow epitaxially. (*(a) and (b) are reproduced from the publication by D. Makovec, N. Križaj, A. Meden, G. Dražić, H. Uršič, R. Kostanjšek, M. Šala, S. Gyergyek, Nanoscale 2022, 14, 3537–3544,*[52] *(c) adapted from the publication by D. Makovec, N. Križaj, S. Gyergyek, CrystEngComm 2022, 24, 3972–398, with permission from The Royal Society of Chemistry.*[52])

(b) shows the HAADF STEM image of a small BIT NPL, oriented edge-on along the [110] direction of its pseudo-tetragonal structure. The two layers of the Aurivillius structure, i.e., a $(Bi_2O_2)^{2+}$ layer and a $(Bi_2Ti_3O_{10})^{2-}$ perovskite-like layer, can be clearly distinguished. The NPL structure always terminates at the large {001} surfaces with the $(Bi_2O_2)^{2+}$ layers. Thus, it is expected that the thin BIT NPLs will be Bi-rich compared to the $Bi_4Ti_3O_{12}$ bulk. However, the BIT NPLs were generally much thicker than the hexaferrite NPLs presented above, usually more than 10 nm thick, so that their actual composition approached to the bulk composition.

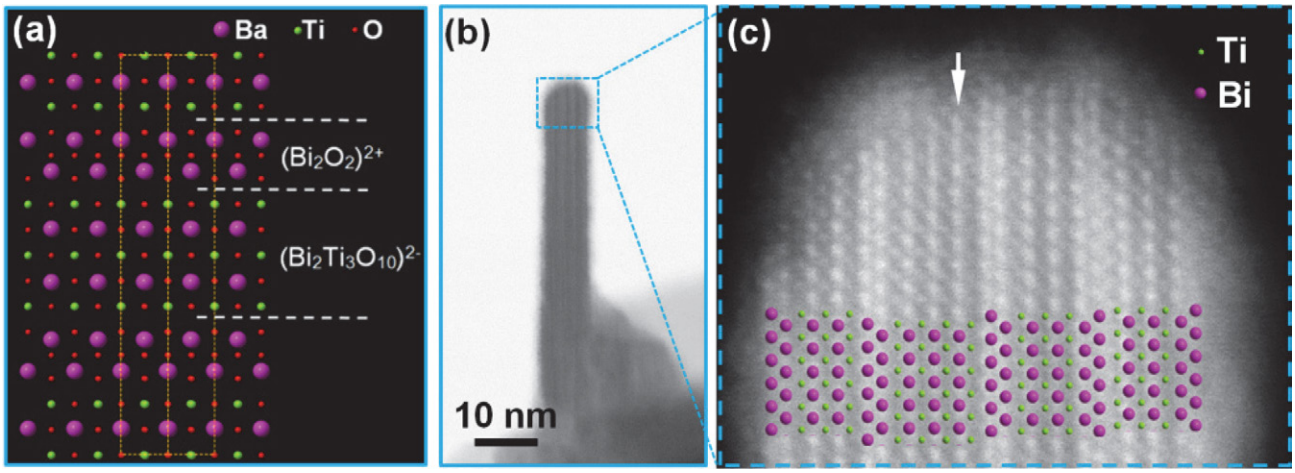

Figure 7. Schematic representation of the magnetoplumbite structure (a), and BF (b) and HAADF (c) STEM images of BIT NPL oriented along [110] direction of the pseudo-tetragonal Aurivillius structure (b). The projected structural models are superimposed over the image (c) to illustrate the positions of the Bi^{3+} and Ti^{4+} ions. The arrow marks a defected perovskite block (*Adapted from the publication by D. Makovec, N. Križaj, S. Gyergyek, CrystEngComm 2022, 24, 3972 – 398, with permission from The Royal Society of Chemistry.*[52])

3. 4. Structure of Bismuth-Titanate Nanowires

The 1-D shape of the NWs, which always form in the initial stages of the hydrothermal synthesis, is not consistent with the layered Aurivillius structure (the pseudo-tetragonal layered structure will tend to form rectangular platelet crystals). Indeed, the XRD of the BIT NWs suggested a new structure, entirely different to the Aurivillius structure characteristic for the BIT.[52] (As explained below, the NW structure does not contain any perovskite-like layers). EDXS analyses showed the same composition for the two BIT morphologies within the uncertainty of the method. The chemical ICP-OES analysis further confirmed the EDXS analyses and showed that sodium from the NaOH used as the mineralizer hydroxide for the synthesis was not incorporated into the NW structure in a significant concentration. Electron diffraction in the TEM suggested an orthorhombic unit cell. Based on the orthorhombic cell and the cell parameters obtained from the electron diffraction it was possible to find a unit cell that gave a satisfactory LeBail fit to the experimental powder XRD pattern with the refined unit-cell parameters: a = 3.804(1) Å, b = 11.816(3) Å, and c = 9.704(1) Å.[53]

Atomic-resolution STEM imaging confirmed that the NWs exhibit a different structure to that of the NPLs. Figure 8 shows HAADF STEM images of NWs oriented normal to the electron beam (in the [010] zone axis) and along the beam (in the [100] zone axis). Based on the HAADF STEM imaging and the analysis of the XRD pattern, a tentative arrangement of the cations in the structure was proposed (Figure 8 (a)). The structure of the NWs is composed of two layers stacked along the c-direction of the orthorhombic unit cell: a layer composed of two parallel rows of Bi atoms in a zig-zag arrangement (marked with "B" in Figure 8 (c)) and a layer of two rows of Ti atoms in a zig-zag arrangement, where every sixth Ti is exchanged with Bi (marked with "T"). The B layer resembles the $(Bi_2O_2)^{2+}$ layer of the Aurivillius structure, while the T layer is much thinner than the perovskite $(Bi_2Ti_3O_{10})^{2-}$ layer of the Aurivillius structure. The arrangement of the Ti atoms in the T layer is consistent with two layers of edge-sharing $(TiO_6)^{2-}$ octahedra, as opposed to the corner-sharing $(TiO_6)^{2-}$ octahedra of the perovskite layers. The proposed cation arrangement in the NW structure predicts a Bi:Ti ratio of 7:5, which deviates from the BIT composition (Bi:Ti = 4:3). The excess Bi, predicted by the model, is most probably compensated by a random partial insertion of the Ti layers parallel to the (010) planes, visible along the [100] direction (Figure 8 (e)).[53]

If the BIT NWs were annealed at high temperature, they transformed to the Aurivillius structure. In the powder obtained by annealing the NWs for 2 hours at 525 °C some nanoparticles were just partially transformed. A HAADF STEM analysis (Figure 9) showed that the transformation of the NW structure to the Aurivillius (AU) structure is topotactic ($(100)_{NW}$ || $(110)_{AU}$, $(001)_{NW}$ || $(001)_{AU}$), $(010)_{NW}$ || $(\bar{1}10)_{AU}$).[53] The analysis also strongly suggested that the transformation does not involve any changes to the composition (the precipitation of secondary phases was not detected). This is a strong indication that the NWs are actually a metastable polymorph of BIT stabilized at the nanoscale. With growth at high temperatures the metastable NW structure transforms to the thermodynamically stable Aurivillius structure.

4. Final Remarks and Future Directions

The chemical composition and the crystal structure of materials tend to define their functional properties. Nowadays, discoveries of entirely new crystal structures of

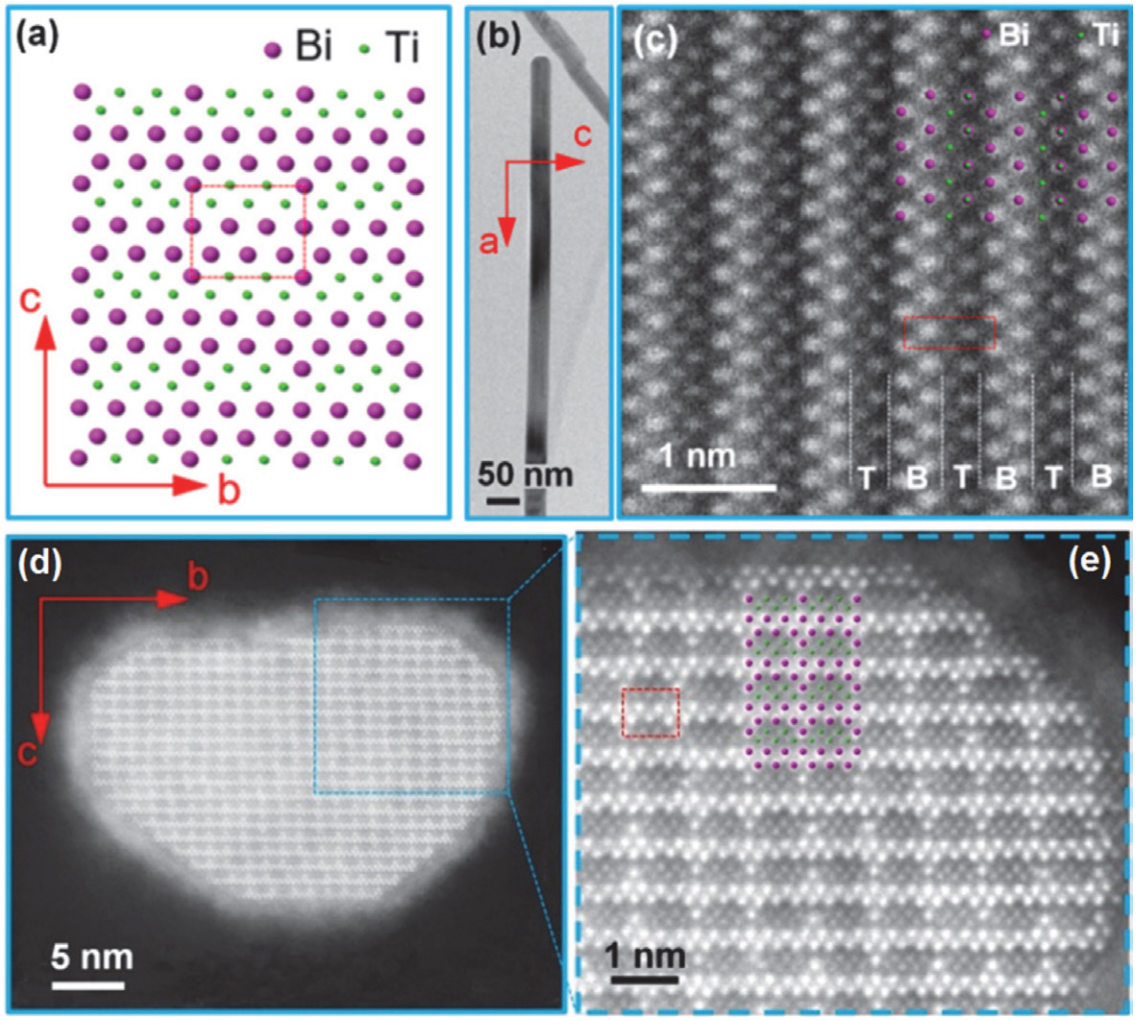

Figure 8. Cation arrangement in a tentative model of an orthorhombic structure of BIT NW (a), TEM (b) and HAADF STEM (c) images of NW oriented along the [010] direction, and HAADF STEM images ((d) and (e)) of NW oriented along the [100] direction of the orthorhombic structure. The projected model proposed for the NW structure is also superimposed over the images (c) and (e) to illustrate the positions of the Bi^{3+} and Ti^{4+} ions. The unit cell of the NW structure is marked with a red rectangle on the HAADF image. (*Adapted from the publication by D. Makovec, N. Križaj, A. Meden, G. Dražić, H. Uršič, R. Kostanjšek, M. Šala, S. Gyergyek, Nanoscale 2022, 14, 3537–3544 with permission from The Royal Society of Chemistry.*[53])

inorganic materials are seldom. However, when materials are synthesized in the form of nanoparticles, their crystal structure can change significantly because of its adaptation to the restricted size. The extent of these structural changes increases with the increasing complexity of the structure. In this article, research at the Department for Materials Synthesis, Jožef Stefan Institute, devoted to the adaptation of complex structures built from alternating layers of two structural blocks to the restricted size of nanoparticles was presented based on two examples of well-known and technologically very important materials, the hexaferrites BHF and SHF, and the Aurivillius layered perovskite, BIT. Both examples confirmed that the nanoparticles with layered structures will normally adopt a plate-like shape and a specific structure defined by a termination at surfaces with a specific, low-energy atomic layer. For a small thickness of the platelet crystal, the structure can significantly deviate from the ordered bulk structure. Moreover, the adaptation of the crystal structure to the restricted size will result in a deviation from the bulk composition. With the defined structure and composition, which are different to those of the bulk, the NPLs can even be considered as new compounds or at least variations of the bulk structures.

The adaptation of the structure to the restricted size will certainly contribute to changed material properties when compared to the bulk properties. This aspect of the size effect has seldom been studied. Since the size has a large effect on the properties per se, it is difficult to estimate the extent of the size effect, which is specifically related to the changed structure. However, there are some indications of positive effects of the structural adaptation on the functional properties of nanoparticles. For example, we can speculate that the SRS^*R^*S-structured hexaferrite NPLs exhibit increased magnetization due to the surface termination with the S block, because the S block has a larger theoretical saturation magnetization

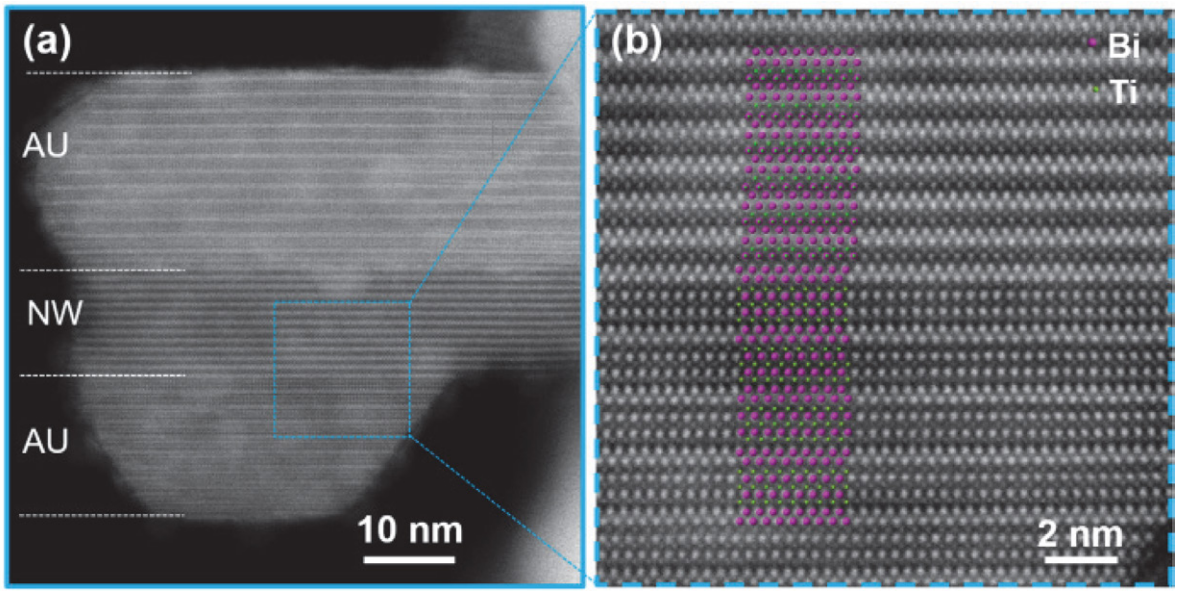

Figure 9. HAADF STEM images of a BIT particle from the NW sample annealed for 2 hours at 525 °C. The particle is composed of a NW sandwiched between two lamellas with the Aurivillius (AU) structure ($[010]_{NW}||[110]_{AU}$). Projected models of the AU structure and the NW structure are superimposed over (b) to illustrate the positions of the Bi^{2+} and Ti^{4+} ions. (*Reproduced from the publication by D. Makovec, N. Križaj, A. Meden, G. Dražić, H. Uršič, R. Kostanjšek, M. Šala, S. Gyergyek, Nanoscale 2022, 14, 3537–3544 with permission from The Royal Society of Chemistry.*[53])

than the R block.[8] We also found one example where the BHF nanoplatelets behave completely differently than the bulk. A partial substitution of Fe^{3+} ions in BHF with Sc^{3+} ions greatly improves the saturation magnetization of the NPLs. The effect was surprising since the substitution of diamagnetic Sc strongly decreases the saturation magnetization of bulk BHF. Ab-initio calculations pointed to a specific, two-dimensional magnetic ordering in the NPLs as the most probable reason for the opposite effect of the Sc substitution in the NPLs to that in the bulk.[44]

The metastable polymorphs, which are frequently obtained because they have a lower nucleation barrier compared to the thermodynamically stable phase, have seldom been considered in the context of size effect, even though they remain stable only while in the form of small particles, i.e., at the nanoscale. Many well-known and technologically very important nanomaterials, e.g., magnetic maghemite nanoparticles and catalytic anatase nanoparticles, are actually metastable polymorphs stabilized on the nanoscale. Interestingly, metastable polymorphs were not reported for complex materials such as mixed oxides with a layered structure. To the best of our knowledge the structure of primary SHF NPLs represented the first reported inorganic metastable polymorph with a complex, layered structure, stabilized at the nanoscale. The NPLs with the newly discovered SHF structure exhibit weak magnetic properties, comparable to those of the SRS*-structured BHF NPLs. Other functional properties, e.g., catalytic, electronic, etc., were not compared. To show that the discovery of a new structure is not only a special case specific for the SHF, we looked for new metastable polymorphs in other well-known materials with a layered structure. The discovery of the new BIT polymorph clearly demonstrated that the metastable polymorphs can generally also be expected to form in mixed oxides with a layered structure. Observations of the ferroelectric domains with TEM and piezo-response force microscopy indicated the ferroelectric nature of the BIT NWs polymorph;[53] however, their functional properties remain to be studied. Nevertheless, the discovery of new polymorphs demonstrated the immense potential of the stabilization of new metastable polymorphs of complex functional materials for the discovery of new nanomaterials. It is possible that a metastable polymorph of a known complex functional material, which will exhibit improved or even entirely new functional properties, could be discovered.

Both aspects of the influence of the size effect on the crystal structure of nanoparticles, i.e., the adaptation of the structure to the restricted size and the stabilization of metastable polymorphs on the nanoscale, are also important in the context of materials synthesis. For example, the adaptation of the hexaferrite structure to the small size of hydrothermally synthesized nanoplatelets will influence the final composition of hexaferrite ceramics after sintering.[54] Moreover, we showed that the metastable polymorphs have an important role in the hydrothermal synthesis of BIT nanoparticles.[52]

Advances in controlled synthesis enabling the synthesis of small nanoparticles of inorganic materials with a complex structure, on the one hand, and the advances in structural characterization based on advanced electron microscopy, on the other, will pave the way to further discoveries of nanoparticles with new and interesting crystal

structures. And with new structures, new properties of the nanoparticles can be expected.

Acknowledgements

I would like to thank my colleagues at the Department for Materials Synthesis, Jožef Stefan Institute, Prof. Dr. Darja Lisjak and Asst. Prof. Dr. Sašo Gyergyek for a fruitful collaboration. The research contribution and experimental help of former and current Ph.D. students and coworkers is also acknowledged: Dr. Darinka Primc, Dr. Blaž Belec, Tanja Goršak, Nina Križaj, and Bernarda Anželak. I am particularly grateful to Prof. Dr. Goran Dražić and other colleague microscopists from the National Institute of Chemistry and Jožef Stefan Institute for their help with the microscopy. I also have to acknowledge Prof. Dr. Matej Komelj from the Department for Nanostructured Materials, Jožef Stefan Institute, Prof. Dr. Layla Martin-Samos, Dr. Matic Poberžnik, and Dr. Gabriela Herrero-Saboya from SISSA, Trieste, for the theoretical considerations, Prof. Dr. Anton Meden from Faculty of Chemistry and Chemical Technology, University of Ljubljana for the XRD analyses of the BIT nanoparticles, Prof. Dr. Rok Kostanjšek from the Biotechnical Faculty, University of Ljubljana, for the help with TEM specimen preparation using microtome, and Dr. Martin Šala from the National Institute of Chemistry for the ICP chemical analyses. The financial support from the Slovenian Research Agency (ARRS) within research core funding No. P2-0089 is greatly appreciated.

5. References

1. G. Guisbiers, *J. Phys. Chem. C* **2011**, 115, 2616–2621. **DOI:**10.1021/jp108041q
2. T. Kamiyama, K. Haneda, T. Sato, S. Ikeda, H. Asano, *Solid State Commun.* **1992**, 81, 563–566. **DOI:**10.1016/0038-1098(92)90412-3
3. S. Calvin, E. E. Carpenter, B. Ravel, V. G. Harris, S. A. Morrison, *Phys. Rev.* **2002**, B66, 224405-1–13. **DOI:**10.1016/0038-1098(92)90412-3
4. D. Makovec, A. Kodre, I. Arčon, M. Drofenik, *J. Nanoparticle Res.* **2008**, 11, 1145–1158. **DOI:**10.1007/s11051-008-9510-0
5. D. Makovec, M. Drofenik, *J. Nanoparticle Res.* **2008**, 10, 131–141. **DOI:**10.1007/s11051-008-9400-5
6. D. Makovec, A. Kodre, I. Arčon, M. Drofenik, *J. Nanoparticle Res.* **2011**, 13, 1781–1790. **DOI:**10.1007/s11051-010-9929-y
7. D. Makovec, B. Belec T. Goršak, D. Lisjak, M. Komelj, G. Dražić, S. Gyergyek, *Nanoscale* **2018**, 10, 14480–14491. **DOI:**10.1039/C8NR03815E
8. B. Belec, G. Dražić, S. Gyergyek, B. Podmiljšak, T. Goršak, M. Komelj, J. Nogués, D. Makovec, *Nanoscale* **2017**, 9, 17551–17560. **DOI:**10.1039/C7NR05894B
9. R. M. Cornell, U. Schwertmann, *The Iron Oxides: Structure, Properties, Reactions, Occurrences and Uses*, Viley-VCH, Weinheim, 2003. **DOI:**10.1002/3527602097
10. I. N. Stranski, D. Totomanow, *Z. Phys. Chem.* **1933**, 163, 399–408. **DOI:**10.1515/zpch-1933-16335
11. A. Navrotsky, *Proc. Natl. Acad. Sci. USA* **2004**, 101, 12096–12101. **DOI:**10.1073/pnas.0404778101
12. S. Sakurai, A. Namai, K. Hashimoto, S. Ohkoshi, *J. Am. Chem. Soc.* **2009**, 131, 18299–18303. **DOI:**10.1021/ja9046069
13. M. Tadić, I. Milosevic, S. Kralj, D. Hanzel, T. Barudžija, L. Motte, D. Makovec, *Acta Mater.* **2020**, 188, 16–22. **DOI:**10.1016/j.actamat.2020.01.058
14. N.T.K. Thanh, Magnetic Nanoparticles From Fabrication to Clincal Applications, CRC Press, Boca Raton, 2012.
15. R. Pullar, *Prog. Mat. Sci.* **2012**, 57, 1191–1334. **DOI:**10.1016/j.pmatsci.2012.04.001
16. A. Mertelj, D. Lisjak, M. Drofenik, M. Čopič, *Nature* 2013, 504, 237–241. **DOI:**10.1038/nature12863
17. M. Shuai, A. Klittnick, Y. Shen, G.P. Smith, M.R. Tuchband, C. Zhu, R.G. Petschek, A. Mertelj, D. Lisjak, M. Čopič, J.E. Maclennan, M.A. Glaser, N.A. Clark, *Nat. Commun.* **2016**, 7, 10394-1–8. **DOI:**10.1038/ncomms10394
18. S.E. Kushnir, A.I. Gavrilov, P.E. Kazin, A.V. Grigorieva, Y.D. Tretyakova, M. Jansen, *J. Mater. Chem.* 2012, 22, 18893–18901. **DOI:**10.1039/c2jm33874b
19. A.A. Eliseev, A.A. Eliseev, L.A. Trusov, A.P. Chumakov, P. Boesecke, E.O. Anokhin, A.V. Vasiliev, A.E. Sleptsova, E.A. Gorbachev, V.V. Korolev, P.E. Kazin, *Appl. Phys. Lett.* **2018**, 113, 13106-1–5. **DOI:**10.1063/1.5044728
20. G. Ferk, P. Kranjc, A. Hamler, A. Mertelj, F. Cebollada, M. Drofenik, D. Lisjak, *Sci. Rep.* **2015**, 5, 11395-1–8. **DOI:**10.1038/srep11395
21. H. Al-Bustami, G. Koplovitz, D. Primc, S. Yochelis, E Capua, D. Porath, R. Naaman, Y. Paltiel, *Small* **2018**, 14, 1801249-1–6. **DOI:**10.1002/smll.201801249
22. G. Koplovitz, D. Primc, O. B. Dor, Shira Y., D. Rotem, D. Porath, Y. Paltiel, *Adv. Mater.* **2017**, 29, 1606748-1–6. **DOI:**10.1002/adma.201606748
23. J. Hu, T. Gorsak, E. Martín Rodríguez, D. Calle, T. Muñoz-Ortiz, D. Jaque, N. Fernández, L. Cussó, F. Rivero, R. Aguilar Torres, J. García Solé, A. Mertelj, D. Makovec, M. Desco, D. Lisjak, F. Alfonso, F. Sanz-Rodríguez, D. H. Ortgies, *ChemPhotoChem* **2019**, 3, 1–12. **DOI:**10.1002/cptc.201900071
24. T. Goršak, M. Drab, D. Križaj, M. Jeran, J. Genova, S. Kralj, D. Lisjak, V. Kralj-Iglič, A. Iglič, D. Makovec, *J. Colloid Interface Sci.* **2020**, 579, 508–519. **DOI:**10.1016/j.jcis.2020.06.079
25. T. Jardiel, A.C. Caballero, M. Villegas, *J. Ceram. Soc. JAPAN* **2008**, 116, 511–518. **DOI:**10.2109/jcersj2.116.511
26. H. Li, L. Su, S. Kuang, Y. Fan, Y. Wu, Z. L. Wang, G. Zhu, *Nano Res.* **2017**, 10, 785–793. **DOI:**10.1007/s12274-016-1331-3
27. J. Hu, Y. Yu, H. Guo, Z. Chen, A. Li, X. Feng, B. Xi, G. Hu, *J. Mater. Chem.* **2011**, 21, 5352–5359. **DOI:**10.1039/c0jm03010d
28. Z. Chen, Y. Yu, H. Guo, J. Hu, *J. Phys. D: Appl. Phys.* **2009**, 42, 125307-1–9. **DOI:**10.1088/0022-3727/42/12/125307
29. T. Xiao, C. Guo, H. Wanga, R. Zhang, Y. Li, W. Shao, Y.

Zhang, X. Wu, J. Tan, W. Ye, *Mater. Lett*. **2020**, 269, 127679-1 – 127679-4. **DOI:**10.1016/j.matlet.2020.127679
30. S. Tu, H. Huang, T. Zhang, Y. Zhang, Appl. Catal., 2017, 219, 550–562. **DOI:**10.1016/j.apcatb.2017.08.001
31. J. Wu, N. Qin, E. Lin, B. Yuan, Z. Kang, D. Bao, *Nanoscale* **2019**, 11, 21128–21136. **DOI:**10.1039/C9NR07544E
32. Q. Yang, Y. Li, Q. Yin, P. Wang, Y.-B. Cheng, *J. Eur. Ceram. Soc.* **2003**, 23, 161–166. **DOI:**10.1016/S0955-2219(02)00087-0
33. N. Plakida, *High-Temperature Cuprate Superconductors: Experiment, Theory, and Applications*, Springer, Berlin, Heidelberg, 2012.
34. M. Zhang, D.A. Kitchaev, Z. Lebens-Higgins, J. Vinckeviciute, M. Zuba, P.J. Reeves, C.P. Grey, M.S. Whittingham, L.F.J. Piper, A. Van der Ven, Y.S. Meng, *Nat. Rev. Mater.* **2022**, 7, 522–540. **DOI:**10.1038/s41578-022-00416-1
35. C. Zhao, Z. Yao, Q. Wang, H. Li, J. Wang, M. Liu, S. Ganapathy, Y. Lu, J. Cabana, B. Li, X. Bai, A. Aspuru-Guzik, M. Wagemaker, L. Chen, Y.-S. Hu, *J. Am. Chem. Soc.* **2020**, 142, 5742–5750. **DOI:**10.1021/jacs.9b13572
36. Y.X. Gan, A.H. Jayatissa, Z. Yu, X. Chen, M. Li, *J. Nanomater.* **2020**, 8917013-1–3. **DOI:**10.1155/2020/8917013
37. A.C.T. Koch, Determination of Core Structure Periodicity and Point Defect Density along Dislocations. Ph.D. Thesis, Arizona State University, 2002.
38. D. Lisjak, A. Mertelj, *Prog. Mater. Sci.* **2018**, 95. 286–328. **DOI:**10.1016/j.pmatsci.2018.03.003
39. D. Primc, D. Makovec, D. Lisjak, M. Drofenik, *Nanotechnology* **2009**, 20, 315605-1–9. **DOI:**10.1088/0957-4484/20/31/315605
40. M. Drofenik, I. Ban, G. Ferk, D. Makovec, A. Žnidaršič, Z. Jagličić, D. Lisjak, *J. Am. Ceram. Soc.* **2010**, 93, 1602–1607. **DOI:**10.1111/j.1551-2916.2010.03620.x
41. D. Primc, M. Drofenik, D. Makovec, *European J. Inorg. Chem.* **2011**, 2011, 3802–3809. **DOI:**10.1002/ejic.201100326
42. D. Lisjak, M. Drofenik, *Cryst. Growth Des.* **2012**, 12, 5174–5179. **DOI:**10.1021/cg301227r
43. C. Granados-Miralles, M. Saura-Múzquiz, E. D. Bøjesen, K. M. Ø. Jensen, H. L. Andersen, M. Christensen, *J. Mater. Chem. C* **2016**, 4, 10903–10913. **DOI:**10.1039/C6TC03803D
44. D. Makovec, M. Komelj, G. Dražić, B. Belec, T. Goršak, S. Gyergyek, D. Lisjak, *Acta Mater.* **2019**, 172, 84–91. **DOI:**10.1016/j.actamat.2019.04.050
45. D. Makovec, G. Dražić, S. Gyergyek, D. Lisjak, *CrystEngComm* **2020**, 22, 7113–7122. **DOI:**10.1039/D0CE01111H
46. D. Makovec, D. Primc, S. Šturm, A. Kodre, D. Hanžel, M. Drofenik, *J. Sol. State Chem.* **2012**, 196, 63–71. **DOI:**10.1016/j.jssc.2012.07.043
47. J. A. Kohn, D. W. Eckart, Jr. F. C. Charles, *Science*, **1971**, 172, 519–525. **DOI:**10.1126/science.172.3983.519
48. M. Poberžnik, G. Herrero-Saboya, D. Lisjak, A. Mertelj, D. Makovec, L. Martin-Samos, Book of Abstracts, SCS Annual Meeting 2022, Portorož, 21–23.9.2022, Slovenian Chemical Society.
49. D. Urushihara, M. Komabuchi, N. Ishizawa, M. Iwata, K. Fukuda, T. Asaka, *J. Appl. Phys.*, **2016**, 120, 142117-1–5. **DOI:**10.1063/1.4961719
50. H. Gu, Z. Hu, Y. Hu, Y. Yuan, J. You, W. Zou, *Colloids Surf. A Physicochem. Eng.* **2008**, 315, 294–298. **DOI:**10.1016/j.colsurfa.2007.08.010
51. F. Wang, J. Wang, X. Zhong, B. Li, J. Liu, D. Wu, D. Mo, D. Guo, S. Yuan, K. Zhang, Y. Zhou, *CrystEngComm* **2013**, 15, 1397–1403. **DOI:**10.1039/c2ce26330k
52. D. Makovec, N. Križaj, S. Gyergyek, *CrystEngComm* **2022**, 24, 3972–3981. **DOI:**10.1039/D2CE00491G
53. D. Makovec, N. Križaj, A. Meden, G. Dražić, H. Uršič, R. Kostanjšek, M. Šala, S. Gyergyek, *Nanoscale* **2022**, 14, 3537–3544. **DOI:**10.1039/D2NR00307D
54. D. Makovec, S. Gyergyek, T. Goršak, B. Belec, D. Lisjak, *J. Eur. Ceram. Soc.* **2019**, 39, 4831–4841. **DOI:**10.1016/j.jeurceramsoc.2019.07.016
55. G. Guisbiers, *J. Phys. Chem. C* **2011**, 115, 2616–2621. **DOI:**10.1021/jp108041q
56. T. Kamiyama, K. Haneda, T. Sato, S. Ikeda, H. Asano, *Solid State Commun.* **1992**, 81, 563–566. **DOI:**10.1016/0038-1098(92)90412-3
57. S. Calvin, E. E. Carpenter, B. Ravel, V. G. Harris, S. A. Morrison, *Phys. Rev.* **2002**, B66, 224405-1–13. **DOI:**10.1016/0038-1098(92)90412-3
58. D. Makovec, A. Kodre, I. Arčon, M. Drofenik, *J. Nanoparticle Res*. **2008**, 11, 1145–1158. **DOI:**10.1007/s11051-008-9510-0
59. D. Makovec, M. Drofenik, *J. Nanoparticle Res.* **2008**, 10, 131–141. **DOI:**10.1007/s11051-008-9400-5
60. D. Makovec, A. Kodre, I. Arčon, M. Drofenik, *J. Nanoparticle Res.* **2011**, 13, 1781–1790. **DOI:**10.1007/s11051-010-9929-y
61. D. Makovec, B. Belec T. Goršak, D. Lisjak, M. Komelj, G. Dražić, S. Gyergyek, *Nanoscale* **2018**, 10, 14480–14491. **DOI:**10.1039/C8NR03815E
62. B. Belec, G. Dražić, S. Gyergyek, B. Podmiljšak, T. Goršak, M. Komelj, J. Nogués, D. Makovec, *Nanoscale* **2017**, 9, 17551–17560. **DOI:**10.1039/C7NR05894B
63. R. M. Cornell, U. Schwertmann, *The Iron Oxides: Structure, Properties, Reactions, Occurrences and Uses*, Viley-VCH, Weinheim, 2003. **DOI:**10.1002/3527602097
64. I. N. Stranski, D. Totomanow, *Z. Phys. Chem.* **1933**, 163, 399–408. **DOI:**10.1515/zpch-1933-16335
65. A. Navrotsky, *Proc. Natl. Acad. Sci. USA* **2004**, 101, 12096–12101. **DOI:**10.1073/pnas.0404778101
66. S. Sakurai, A. Namai, K. Hashimoto, S. Ohkoshi, *J. Am. Chem. Soc.* **2009**, 131, 18299–18303. **DOI:**10.1021/ja9046069
67. M. Tadić, I. Milosevic, S. Kralj, D. Hanzel, T. Barudžija, L. Motte, D. Makovec, *Acta Mater.* **2020**, 188, 16–22. **DOI:**10.1016/j.actamat.2020.01.058
68. N.T.K. Thanh, Magnetic Nanoparticles From Fabrication to Clincal Applications, CRC Press, Boca Raton, 2012.
69. R. Pullar, *Prog. Mat. Sci.* **2012**, 57, 1191–1334. **DOI:**10.1016/j.pmatsci.2012.04.001
70. A. Mertelj, D. Lisjak, M. Drofenik, M. Čopič, *Nature* 2013, 504, 237–241. **DOI:**10.1038/nature12863
71. M. Shuai, A. Klittnick, Y. Shen, G.P. Smith, M.R. Tuchband, C. Zhu, R.G. Petschek, A. Mertelj, D. Lisjak, M. Čopič, J.E. Maclennan, M.A. Glaser, N.A. Clark, *Nat. Commun.* **2016**, 7, 10394-1–8. **DOI:**10.1038/ncomms10394

72. S.E. Kushnir, A.I. Gavrilov, P.E. Kazin, A.V. Grigorieva, Y.D. Tretyakova, M. Jansen, *J. Mater. Chem.* 2012, 22, 18893–18901. **DOI:**10.1039/c2jm33874b
73. A.A. Eliseev, A.A. Eliseev, L.A. Trusov, A.P. Chumakov, P. Boesecke, E.O. Anokhin, A.V. Vasiliev, A.E. Sleptsova, E.A. Gorbachev, V.V. Korolev, P.E. Kazin, *Appl. Phys. Lett.* **2018**, 113, 13106-1–5. **DOI:**10.1063/1.5044728
74. G. Ferk, P. Kranjc, A. Hamler, A. Mertelj, F. Cebollada, M. Drofenik, D. Lisjak, *Sci. Rep.* **2015**, 5, 11395-1–8. **DOI:**10.1038/srep11395
75. H. Al-Bustami, G. Koplovitz, D. Primc, S. Yochelis, E Capua, D. Porath, R. Naaman, Y. Paltiel, *Small* **2018**, 14, 1801249-1–6. **DOI:**10.1002/smll.201801249
76. G. Koplovitz, D. Primc, O. B. Dor, Shira Y., D. Rotem, D. Porath, Y. Paltiel, *Adv. Mater.* **2017**, 29, 1606748-1–6. **DOI:**10.1002/adma.201606748
77. J. Hu, T. Gorsak, E. Martín Rodríguez, D. Calle, T. Muñoz-Ortiz, D. Jaque, N. Fernández, L. Cussó, F. Rivero, R. Aguilar Torres, J. García Solé, A. Mertelj, D. Makovec, M. Desco, D. Lisjak, F. Alfonso, F. Sanz-Rodríguez, D. H. Ortgies, *ChemPhotoChem* **2019**, 3, 1–12. **DOI:**10.1002/cptc.201900071
78. T. Goršak, M. Drab, D. Križaj, M. Jeran, J. Genova, S. Kralj, D. Lisjak, V. Kralj-Iglič, A. Iglič, D. Makovec, *J. Colloid Interface Sci.* **2020**, 579, 508–519. **DOI:**10.1016/j.jcis.2020.06.079
79. T. Jardiel, A.C. Caballero, M. Villegas, *J. Ceram. Soc. JAPAN* **2008**, 116, 511–518. **DOI:**10.2109/jcersj2.116.511
80. H. Li, L. Su, S. Kuang, Y. Fan, Y. Wu, Z. L. Wang, G. Zhu, *Nano Res.* **2017**, 10, 785–793. **DOI:**10.1007/s12274-016-1331-3
81. J. Hu, Y. Yu, H. Guo, Z. Chen, A. Li, X. Feng, B. Xi, G. Hu, *J. Mater. Chem.* **2011**, 21, 5352–5359. **DOI:**10.1039/c0jm03010d
82. Z. Chen, Y. Yu, H. Guo, J. Hu, *J. Phys. D: Appl. Phys.* **2009**, 42, 125307-1–9. **DOI:**10.1088/0022-3727/42/12/125307
83. T. Xiao, C. Guo, H. Wanga, R. Zhang, Y. Li, W. Shao, Y. Zhang, X. Wu, J. Tan, W. Ye, *Mater. Lett*. **2020**, 269, 127679-1 – 127679-4. **DOI:**10.1016/j.matlet.2020.127679
84. S. Tu, H. Huang, T. Zhang, Y. Zhang, Appl. Catal., 2017, 219, 550–562. **DOI:**10.1016/j.apcatb.2017.08.001
85. J. Wu, N. Qin, E. Lin, B. Yuan, Z. Kang, D. Bao, *Nanoscale* **2019**, 11, 21128–21136. **DOI:**10.1039/C9NR07544E
86. Q. Yang, Y. Li, Q. Yin, P. Wang, Y.-B. Cheng, *J. Eur. Ceram. Soc.* **2003**, 23, 161–166. **DOI:**10.1016/S0955-2219(02)00087-0
87. N. Plakida, *High-Temperature Cuprate Superconductors: Experiment, Theory, and Applications*, Springer, Berlin, Heidelberg, 2012.
88. M. Zhang, D. A. Kitchaev, Z. Lebens-Higgins, J. Vinckeviciute, M. Zuba, P.J. Reeves, C.P. Grey, M. S. Whittingham, L. F. J. Piper, A. Van der Ven, Y. S. Meng, *Nat. Rev. Mater.* **2022**, 7, 522–540. **DOI:**10.1038/s41578-022-00416-1
89. C. Zhao, Z. Yao, Q. Wang, H. Li, J. Wang, M. Liu, S. Ganapathy, Y. Lu, J. Cabana, B. Li, X. Bai, A. Aspuru-Guzik, M. Wagemaker, L. Chen, Y.-S. Hu, *J. Am. Chem. Soc.* **2020**, 142, 5742–5750. **DOI:**10.1021/jacs.9b13572
90. Y. X. Gan, A. H. Jayatissa, Z. Yu, X. Chen, M. Li, *J. Nanomater.* **2020**, 8917013-1–3. **DOI:**10.1155/2020/8917013
91. A.C.T. Koch, Determination of Core Structure Periodicity and Point Defect Density along Dislocations. Ph.D. Thesis, Arizona State University, 2002.
92. D. Lisjak, A. Mertelj, *Prog. Mater. Sci.* **2018**, 95. 286–328. **DOI:**10.1016/j.pmatsci.2018.03.003

Povzetek

Uporabne lastnosti materialov so v veliki meri določene s sestavo in kristalno strukturo materialov. Struktura materiala in posledično tudi njegova sestava se lahko znatno spremenita, če material pripravimo v obliki nanodelcev. Poznavanje sprememb v kristalni strukturi zaradi končne dimenzije nanomaterialov je torej pomembno tako s stališča širjenja osnovnega znanja, kot tudi za načrtovanje novih nanomaterialov za uporabo v tehnologiji in medicini. Spremembe v strukturi so lahko posledica dveh različnih pojavov: (i) kristalna struktura se prilagodi končni velikosti nanodelcev, in (ii) z majhno velikostjo delcev lahko stabiliziramo različne metastabilne strukturne polimorfe, ki nastanejo med sintezo v tekočem zaradi nižje energijske pregrade za nukleacijo v primerjavi z energijsko pregrado potrebno za nukleacijo ravnotežnih faz. Omenjene spremembe v kristalni strukturi so posebej pogoste pri anorganskih materialih s kompleksno strukturo in sestavo, kot so zmesni oksidi s plastovito strukturi sestavljeno iz več strukturnih blokov. Pričujoči članek pojasnjuje kompleksno strukturo nanodelcev na primerih dveh dobro znanih in tehnološko zelo pomembnih materialov s plastovito strukturo: magnetnih heksaferitov ($BaFe_{12}O_{19}$ in $SrFe_{12}O_{19}$) in feroelektričnega bizmutovega titanata ($Bi_4Ti_3O_{12}$) s plastovito perovskitno strukturo Aurivilliusovega tipa.